

# DeepSEED: 3D Squeeze-and-Excitation Encoder-Decoder ConvNets for Pulmonary Nodule Detection

Yuemeng Li, Hangfan Liu, and Yong Fan

Center for Biomedical Image Computing and Analysis, University of Pennsylvania  
ymli@seas.upenn.edu, Yong.Fan@uphs.upenn.edu

**Abstract.** Pulmonary nodule detection plays an important role in lung cancer screening with low-dose computed tomography (CT) scans. Although promising performance has been achieved by deep learning based nodule detection methods, it remains challenging to build nodule detection networks with good generalization performance due to unbalanced positive and negative samples. In order to overcome this problem and further improve state-of-the-art region proposal network methods, we develop a novel deep 3D convolutional neural network with an Encoder-Decoder structure for pulmonary nodule detection. Particularly, we utilize a dynamically scaled cross entropy loss to reduce the false positive rate and compensate the significant data imbalance problem. We adopt the squeeze-and-excitation structure to learn effective image features and fully utilize channel inter-dependency. We have validated our method based on publicly available CT scans from LIDC/IDRI dataset and its subset LUNA16 with thinner slices. Ablation studies and experimental results have demonstrated that our method could outperform state-of-the-art nodule detection methods by a large margin, with an average FROC score of 86.2% on LUNA16, and an average FROC score of 77.3% on LIDC/IDRI dataset when trained on LUNA16 only. Code is available <sup>1</sup>.

**Keywords:** Deep 3D convolutional networks, squeeze-and-excitation, encoder-decoder, lung nodule detection

## 1 Introduction

Lung cancer is one of the most commonly diagnosed cancers in the united states and worldwide [4]. Lung cancer screening with low-dose computed tomography (CT) scans is an effective way to reduce mortality of lung cancer, which relies on accurate pulmonary nodule detection [7]. To achieve accurate and effective pulmonary nodule detection in low-dose CT scans, a number of computer-aid detection (CAD) methods have been developed to detect pulmonary nodules

<sup>1</sup><https://github.com/ymli39/DeepSEED-3D-ConvNets-for-Pulmonary-Nodule-Detection>

using convolutional neural networks (CNNs) [18,8,11,2], following the success of CNN features in a variety of object detection problems [5,14,13].

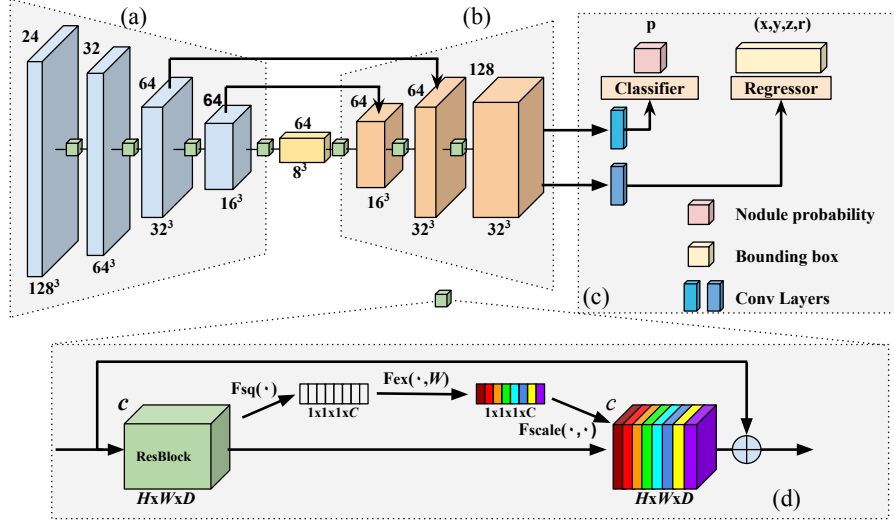
Although the deep learning based methods approach the pulmonary nodule detection problem in many different ways [16,2,3,9,11,18], most of them adopt a two-stage strategy [5], consisting of 1) nodule candidate detection to identify nodule regions with reduced false positive (FP) in a classification setting; and 2) nodule bounding boxes prediction to estimate spatial locations of positive nodules in a regression setting. For instance, a 2D CNN was adopted to build pulmonary nodule detection models on multiple views of 2D CT slices [16], and a 3D CNN model was trained with an online sample filtering scheme for candidate screening, in conjunction with a residual network for FP reduction [3]. Due to their multi-stage frameworks, those methods are computationally expensive and their final outputs might unfavorably depend on their early stage’s performance.

Recent studies have demonstrated that effective and efficient pulmonary nodule detection could be achieved by end-to-end learning methods. Particularly, a nodule detection network has been trained in an end-to-end manner using 3D CNNs [9]. In addition, several pulmonary nodule detection methods have been developed by adopting faster R-CNN which consists of a region proposal network (RPN) to generate region proposals and a detection network to detect objects from proposals [15]. In particular, a 2D faster R-CNN model has been built for candidate detection followed by a 3D CNN for FP reduction [2], a faster R-CNN model has been built upon a 3D RPN with an encoder-decoder structure [11], and a faster R-CNN model with dual path blocks has been built to take the advantages of residual learning and dense connection for accurate nodule detection [18]. In all these methods, nodule candidate detection is the most challenging problem due to the unbalanced sample problem, *i.e.*, a large number of negative samples versus a relatively small number of positive samples.

To achieve improved pulmonary nodule detection in low-dose CT scans, we develop a novel deep Squeeze-and-Excitation Encoder-Decoder (DeepSEED) network to detect nodules in one single step. Particularly, DeepSEED is built upon a 3D RPN with a squeeze-and-excitation structure [6] to effectively learn image features for accurately detecting nodules, DeepSEED’s RPN is built upon an Encoder-Decoder structure to effectively utilized multiscale context image information, and DeepSEED’s RPN utilizes a dynamically scaled cross entropy loss, namely focal loss [12], to compensate the imbalance of positive and negative samples. We have evaluated our method and compared it with state-of-the-art methods based on large data sets, including LIDC/IDRI dataset and its subset LUNA16 with thinner slices. Extensive validation experimental results have demonstrated that our method could achieve much better nodule detection performance than the alternative methods under comparison.

## 2 Methods

The proposed DeepSEED network for automatic pulmonary nodule detection in low-dose CT scans is illustrated by Fig. 1. Specifically, DeepSEED is built



**Fig. 1.** The architecture of DeepSEED. Numbers on the top left of each block indicate the number of channels and those on the bottom right indicate spatial dimensions of input feature maps. (a) An encoder with a 3D ResNet 18 structure. Each down-sampling block is implemented by max-pooling with a stride of 2. (b) A decoder with its feature dimension expanded after the second skip connection. (c) A region proposal network for identifying candidate nodules and predicting their bounding boxes. (d) The squeeze-and-excitation (SE) [6] residual blocks that are adopted in all convolutional blocks in (a) and (b). For each residual block, a SE structure is utilized before each skip connection. Each residual block is squeezed into a  $C$  dimension feature matrix (white blocks) and passes through a gating mechanism that adds spatial encoding (color blocks) to the residual block, with different colors indicating different weights.

upon a 3D region proposal network (RPN) [15] with an Encoder-Decoder structure, enhanced by a Squeeze-and-Excitation structure [6] to fully exploit image features and a focal loss [12] to find true positives among all nodule candidates.

## 2.1 Network Structure

In this study, we adopt a 3D RPN structure as backbone due to its outstanding performance in nodule detection tasks [11,18]. The backbone contains a Res18 structure as the encoder illustrated by Fig. 1(a), and decoder consists of 3 layers residual blocks with skip connections as illustrated by Fig. 1(b). The full network structure is demonstrated in supplementary material. Each residual block contains a Squeeze-and-Excitation unit as shown in Fig. 1(d). The RPN's input is a 3D CT image with anchors that are candidate nodule bounding boxes, and its output includes each anchor's classification probability score  $p$  to be a nodule and the nodule's spatial information including its coordinates  $x, y, z$  and the nodule radius  $r$ . The anchor's size could be set according to the distribution of

nodule sizes of training data. Implementation details are presented in Section of Experiments and results.

To precisely identity the location of the nodules, we adopt a Squeeze-and-Excitation (SE) structure in our network due to its success in image classification [6]. Particularly, the SE could effectively utilize channel inter-dependency with an enhanced spatial encoding to make the network to adaptively adjust the weights of each feature map for the nodule detection tasks. As illustrated by Fig. 1(d), for each convolutional layer, we set  $U = F(X)$ , where  $X$  is the input feature,  $U$  is the output feature matrix after convolution.  $U = [u_1, u_2, \dots, u_n]$  contains the parameters of the  $c$ -th channel. In order to *squeeze* the global spatial information into a channel descriptor, we use channel-wise global average pooling. The output is denoted as  $z_c = F_{sq}(u_c)$ , where the statistic  $\mathbf{z} \in \mathbb{R}^C$  is generated by squeezing  $U$  through the spatial dimensions of  $H \times W \times D$  and  $z_c$  is the  $c$ -th element of  $\mathbf{z}$ .

The channel-wise output of the *squeeze* operation is used to modulate inter-dependencies of all channels through *excitation*, a gating mechanism with a sigmoid activation:

$$s = F_{ex}(u_c) = \sigma(g(z, W)) = \sigma(W_2 \delta(W_1 z)), \quad (1)$$

where  $\delta$  is the ReLU function [10],  $W_1 \in \mathbb{R}^{\frac{C}{r} \times C}$  contains parameters for the dimensionality-reduction layers, and  $W_2 \in \mathbb{R}^{C \times \frac{C}{r}}$  consists of parameters for the dimensionality-increasing layers, with  $r = 16$  [6].

A channel-wised multiplication  $F_{scale}$  between each *excitation* scalar  $s_c$  and the feature map  $u_c$  is finally applied to generate the final re-scaling feature output  $U$ :

$$U = F_{scale}(u_c, s_c) = s_c \cdot u_c, \quad (2)$$

where  $u_c \in \mathbb{R}^{H \times W \times D}$ . The output features of squeeze-and-excitation are obtained before the identity shortcut connection for each residual block.

## 2.2 Classification and Regression Loss

The RPN is trained to minimize a nodule classification loss  $L_{cls}$  and a regression loss for bounding boxes  $L_{reg}$ . To compensate the large imbalance of positive and negative samples of nodule regions and to correct misclassified samples, we adopt a focal loss [12] to compute the nodule classification loss  $L_{cls}$ . Given a positive sample's classification output probability  $p$ , the focal loss function is defined as:

$$L_{cls} = -\alpha(1 - p_t)^\gamma \log(p_t), \quad (3)$$

where  $p_t = p$  if ground truth class label  $y = 1$ , otherwise  $p_t = 1 - p$ .  $\alpha$  is a balance variant for the focal loss, and  $\gamma$  is a tunable *focusing* parameter. In our study,  $\alpha = 0.5$  and  $\gamma = 2$  as suggested by [12].

The regression loss is defined as:

$$L_{reg} = \sum_k S(G_k, P_k), \quad (4)$$

where  $S$  is the smoothed  $\ell_1$ -norm function [15],  $G_k = (\frac{x_g - x_a}{r_a}, \frac{y_g - y_a}{r_a}, \frac{z_g - z_a}{r_a}, \log(\frac{r_g}{r_a}))$  is the parameterized ground truth,  $P_k = (\frac{x - x_a}{r_a}, \frac{y - y_a}{r_a}, \frac{z - z_a}{r_a}, \log(\frac{r}{r_a}))$  is the corresponding parameterized prediction, and  $k$  is an index of anchors in a mini-batch.

The overall loss function is written as:

$$L = L_{cls} + p^* L_{reg}, \quad (5)$$

where  $p^*$  is 1 for positive samples and 0 for negative samples.

### 3 Experiments and Results

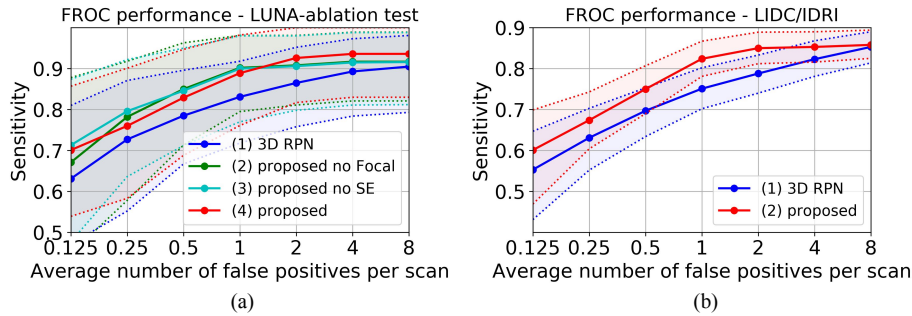
We compared our method with state-of-the-art nodule detection methods built upon RPNs [11,18]. Particularly, a 3D RPN [11] was adopted as the baseline and we further compared our results with Dual Path Network [18] due to its outstanding performance on LUNA16 dataset.

**Dataset:** We used publicly available LIDC/IDRI dataset [1] and its subset LUNA16 [17] to evaluate the nodule detection methods under comparison. Both the datasets labeled nodules greater than 3 mm. CT scans of LUNA16 and LIDC/IDRI differ mainly in their slice thickness. LUNA16 contains 888 cases of CT scans with 1186 labeled nodules, obtained from LIDC dataset by excluding CT scans with slice thickness greater than 2.5 mm. Another noticeable difference between LUNA16 and LIDC/IDRI is their nodule size distribution. The mean nodule size of LUNA16 is 8.3 mm with a variance of 4.8 mm whereas that of LIDC/IDRI is 12.8 mm with a variance of 10.6 mm. Nodule detection is more challenging on LIDC/IDRI dataset because of its lower spatial resolution. We used a 10-fold cross-validation on LUNA16 to evaluate our method, and tested DeepSEED’s robustness on external 122 subjects from LIDC/IDRI dataset (excluding LUNA16).

**Implementation Details:** We preprocessed each input image with a binary segmentation mask to segment lungs, and clipped pixel values to the range  $[-1200, 600]$ , then normalized them to  $[0, 1]$ . We divided images into patches of  $128 \times 128 \times 128$  as the network input for training. All the patches were randomly cropped, and additional data augmentation was implemented with random flipping and scaling with the ratio ranging 0.75 to 1.25. To generate training anchors, boxes with Intersection over Union (IoU) greater than 0.5 were defined as positive samples and smaller than 0.02 as negative samples. The anchors with the size of  $[5, 10, 20]$  are selected. For testing, we divided images into patches of size  $208 \times 208 \times 208$  with an overlapping of 32 pixels for neighboring patches. The model performance was evaluated using an official script of Free-Response Receiver Operating Characteristic (FROC) analysis provided by LUNA16 [17]. In the FROC analysis, sensitivity is defined as a function of the average number of false positives per scan (FPs/scan). The overall score was evaluated at 0.125, 0.25, 0.5, 1, 2, 4 and 8 false positives per scan. We trained our network on 8 NVIDIA 1080Ti GPUs with the batch size of 40.

**Table 1.** FROC (%) comparisons on LUNA and LIDC/IDRI datasets. The first three rows with gray colored background are results on LUNA dataset, and the last two rows are results on LIDC/IDRI dataset.

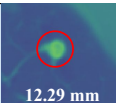
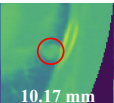
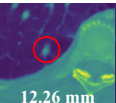
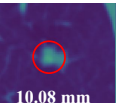

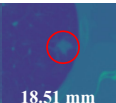
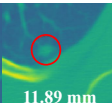
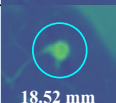
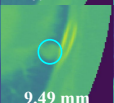
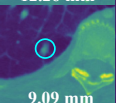
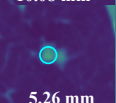
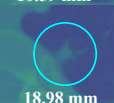
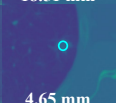
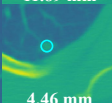

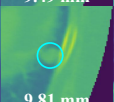
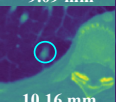
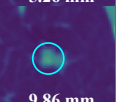
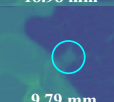
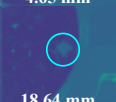
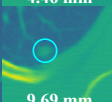
FROC	0.125	0.25	0.5	1	2	4	8	Mean
3D RPN[11]	0.662	0.746	0.815	0.864	0.902	<b>0.918</b>	0.932	0.834
DeepLung[18]	0.692	0.769	0.824	0.865	0.893	0.917	<b>0.933</b>	0.842
DeepSeed(ours)	<b>0.739</b>	<b>0.803</b>	<b>0.858</b>	<b>0.888</b>	<b>0.907</b>	0.916	0.920	<b>0.862</b>
3D RPN[11]	0.552	0.630	0.700	0.751	0.788	0.823	0.852	0.728
DeepSeed(ours)	<b>0.600</b>	<b>0.674</b>	<b>0.751</b>	<b>0.824</b>	<b>0.850</b>	<b>0.853</b>	<b>0.859</b>	<b>0.773</b>



**Fig. 2.** FROC curves obtained from a randomly selected fold. The dash-lines show the corresponding upper and lower bounding after bootstrapping. (a) Comparison of different models for ablation studies on LUNA16 dataset. (b) Comparison of 3D Res18 backbone and DeepSEED on LIDC/IDRI dataset.

**Network Performance:** We implemented 3D RPN [11] as our baseline, and compared our results on LUNA 16 dataset with those reported in DeepLung [18], as summarized in Table 1. We randomly shuffle the dataset into 10 folds with performance of each fold shown in supplementary material. These results demonstrated that our network improved the 3D RPN and DeepLung in terms of average FROC score by 2.8% and 2% on LUNA 16 dataset respectively, and our network improved the 3D RPN in terms of average FROC score by 4.5% on LIDC/IDRI dataset, as illustrated by Fig. 2(b). Our model especially outperformed the state-of-the-art nodule detection methods by a large margin for the settings of average numbers of FPs/scan smaller than 2. The results on LIDC/IDRI dataset also indicated that our network had a better generalization performance since our network was trained on LUNA16.

**Ablation study:** This ablation was performed on a randomly selected fold. We compared the 3D RPN with DeepSEED and its degraded versions without focal loss (proposed no Focal) and without SE blocks (proposed no SE). As illustrated by results shown in Fig. 2(a), the sensitivity of RPN was much lower than DeepSEED and its degraded versions. For settings of average numbers of FPs/scan smaller than or equal to 1, the degraded versions of DeepSEED

Ground Truth Center Slice							
	12.29 mm	10.17 mm	12.26 mm	10.08 mm	10.59 mm	18.51 mm	11.89 mm
3D RPN Center Slice							
	18.52 mm	9.49 mm	9.09 mm	5.26 mm	18.98 mm	4.65 mm	4.46 mm
DeepSeed Center Slice							
	10.10 mm	9.81 mm	10.16 mm	9.86 mm	9.79 mm	18.64 mm	9.69 mm

**Fig. 3.** Visualization of nodule detection results obtained by the 3D RPN and DeepSEED on representative LIDC/IDRI scans (from left to right). Nodule images are displayed in the axial view, including corresponding diameter values on the bottom of each bounding box. From top to bottom: (a) ground truth bounding boxes; (b) bounding boxes obtained by the 3D RPN; (c) Bounding boxes generated by DeepSEED.

achieved better score, but DeepSEED had better performance for settings of average numbers of FPs/scan greater than 1. These experimental results indicated that both the SE structure and the focal loss could improve the 3D RPN’s performance if they were used alone, and their combination could further improve the 3D RPN’s performance for setting of average numbers of FPs/scan greater than 1. In particular, we expect the model to generate precise locations and sizes of bounding boxes with the incorporation of SE structure and focal loss.

**Major Findings:** (1) Our proposed DeepSEED achieved the highest average FROC score of **86.2%** on LUNA16 and **77.3%** on LIDC/IDRI; (2) DeepSEED outperformed 3D RPN [11] and DeepLung [18] on LUNA16 dataset in terms of average FROC scores by **4.1%** and **3.0%** on 0.125 to 2 false positives per scan respectively; (3) the incorporation of the SE and focal loss improved the overall performance of the network; (4) DeepSEED yielded not only accurate bounding boxes locations but also precise bounding boxes sizes, as illustrated by results shown in Fig. 3.

## 4 Conclusion

In this study, we have developed a novel End-to-End Encoder-Decoder deep 3D Squeeze-and-Excitation (SE) ConvNet for pulmonary nodules detection in low-dose lung CT scans. To overcome problems caused by sample imbalance and further reduce the false positive rate, our network adopted a focal classification loss in the proposed network. Our network was further improved by the Squeeze-and-Excitation (SE) structures. The ablation studies have demonstrated both the focal loss and SE structures could improve the baseline method, namely 3D RPN. We trained our model on LUNA16 and tested it on both LUNA16 and a subset of LIDC/IDRI dataset with thicker slices than those of LUNA 16 scans.

On both the datasets, our model has achieved evident improvement over current state-of-the-art methods with the same network backbone.

## References

1. Armato III, S.G., McLennan, G., Bidaut, L., et al.: The lung image database consortium (lidc) and image database resource initiative (idri): a completed reference database of lung nodules on ct scans. *Medical Physics* **38**(2), 915–931 (2011)
2. Ding, J., Li, A., Hu, Z., Wang, L.: Accurate pulmonary nodule detection in computed tomography images using deep convolutional neural networks. In: *International Conference on MICCAI*. pp. 559–567. Springer (2017)
3. Dou, Q., Chen, H., Jin, Y., et al.: Automated pulmonary nodule detection via 3d convnets with online sample filtering and hybrid-loss residual learning. In: *International Conference on MICCAI*. pp. 630–638. Springer (2017)
4. Ferlay, J., Soerjomataram, I., Dikshit, R., et al.: Cancer incidence and mortality worldwide: sources, methods and major patterns in globocan 2012. *International Journal of Cancer* **136**(5), E359–E386 (2015)
5. Girshick, R., Donahue, J., Darrell, T., Malik, J.: Rich feature hierarchies for accurate object detection and semantic segmentation. In: *Proceedings of the IEEE Conference on CVPR*. pp. 580–587 (2014)
6. Hu, J., Shen, L., Sun, G.: Squeeze-and-excitation networks. *arXiv preprint arXiv:1709.01507* **7** (2017)
7. Hunink, M.M., Gazelle, G.S.: Ct screening: a trade-off of risks, benefits, and costs. *The Journal of Clinical Investigation* **111**(11), 1612–1619 (2003)
8. Jin, D., Xu, Z., Tang, Y., Harrison, A.P., Mollura, D.J.: Ct-realistic lung nodule simulation from 3d conditional generative adversarial networks for robust lung segmentation. In: *International Conference on MICCAI* (2018)
9. Khosravan, N., Bagci, U.: S4nd: Single-shot single-scale lung nodule detection. In: *International Conference on MICCAI*. pp. 794–802. Springer (2018)
10. LeCun, Y., Bengio, Y., Hinton, G.: Deep learning. *Nature* **521**(7553), 436 (2015)
11. Liao, F., Liang, M., Li, Z., Hu, X., Song, S.: Evaluate the malignancy of pulmonary nodules using the 3d deep leaky noisy-or network. *CoRR* **abs/1711.08324** (2017)
12. Lin, T.Y., Goyal, P., Girshick, R., He, K., Dollár, P.: Focal loss for dense object detection. *IEEE Transactions on PAMI* (2018)
13. Liu, W., Anguelov, D., Erhan, D., et al.: Ssd: Single shot multibox detector. In: *European conference on computer vision*. pp. 21–37. Springer (2016)
14. Redmon, J., Divvala, S., Girshick, R., Farhadi, A.: You only look once: Unified, real-time object detection. In: *Proceedings of the IEEE conference on computer vision and pattern recognition*. pp. 779–788 (2016)
15. Ren, S., He, K., Girshick, R., Sun, J.: Faster r-cnn: Towards real-time object detection with region proposal networks. In: *Advances in neural information processing systems*. pp. 91–99 (2015)
16. Setio, A.A.A., Ciompi, F., Litjens, G., et al.: Pulmonary nodule detection in ct images: false positive reduction using multi-view convolutional networks. *IEEE Transactions on Medical Imaging* **35**(5), 1160–1169 (2016)
17. Setio, A.A.A., Traverso, A., De Bel, T., et al.: Validation, comparison, and combination of algorithms for automatic detection of pulmonary nodules in computed tomography images: the luna16 challenge. *Medical Image Analysis* **42**, 1–13 (2017)



18. Zhu, W., Liu, C., Fan, W., Xie, X.: Deeplung: Deep 3d dual path nets for automated pulmonary nodule detection and classification. In: IEEE WACV. pp. 673–681 (2018)